JACS
JOURNAL OF THE AMERICAN CHEMICAL SOCIETY
pubs.acs.org/JACS
Article

Heterocyclic-N-Coordinated $Ag_2^{\delta-}$ Monolayer Self-Assembled on Ag(100)

Xiaoshuai Fu,[⧖] Li Huang,*[,⧖] Linlu Wu,[⧖] Yubin Fu,[⧖] Xiao Chang, Xiaoxiao Pei, Chuqi Zhang, Chen Liu, Fupin Liu, Zhihai Cheng, Ji Ma, Xiao Lin, Wei Ji,* Xinliang Feng,* and Hong-Jun Gao

Cite This: https://doi.org/10.1021/jacs.6c00947
Read Online
ACCESS | Metrics & More | Article Recommendations | Supporting Information

ABSTRACT: The charge states of metal adatoms on surfaces play a crucial role in controlling adsorption and interaction behaviors that underpin surface chemistry and catalysis, yet the atomically precise synthesis of negatively charged metal atoms remains a significant challenge. Here, we report negatively charged Ag dimer ($Ag_2^{\delta-}$) arrays assembled on Ag(100) surface through coordination with a polycyclic aromatic hydrocarbon, 8,9-diaza-8a-borabenzo[*fg*]tetracene (DBT), featuring a doping moiety with N−B−N bonds at zigzag edge. The Ag dimers are stabilized by two DBT monomers through N−Ag−N coordination bonding. In contrast to surface Ag atoms, the coordinated dimers display anionic character, as demonstrated by noncontact atomic force microscopy, Kelvin probe force microscopy, X-ray photoelectron spectroscopy, and density functional theory calculations. Neutral dimers Ag_2^0 can be converted from the coordinated complex by tip-induced detachment of one DBT monomer and showed markedly higher affinity for CO adsorption, a process that is suppressed on $Ag_2^{\delta-}$. These findings establish an atomically defined platform for stabilizing and controlling anionic metal centers on metallic surfaces, providing a model system for exploring charge-state effects in surface chemistry.

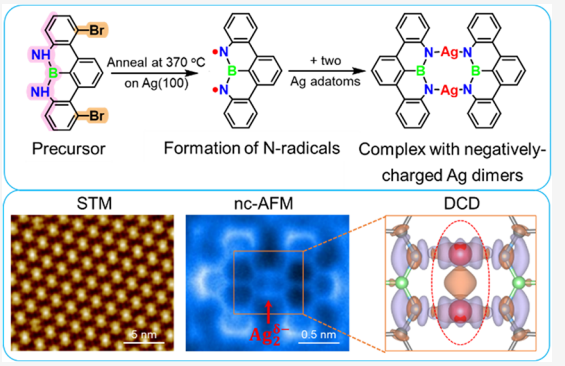

INTRODUCTION

The charge states of metal adatoms on surfaces play a decisive role in governing adsorption energetics, reaction pathways, and catalytic selectivity at the atomic scale.[1−8] While single-atom catalysis (SAC) has demonstrated remarkable activity and selectivity in a wide range of metals and supports, coordination with electronegative ligands such as O, N, or S tends to stabilize cationic or partially oxidized metal centers.[9−13] In contrast, atomically well-defined metal centers with an unambiguous anionic character remain exceedingly rare. This pronounced asymmetry in charge-state accessibility has fundamentally limited the exploration of negatively charged metal sites and their distinct interactions with electrophilic adsorbates.[14]

The scarcity of anionic metal adatoms does not stem from a lack of conceptual interest,[15,16] but rather from synthetic and characterization constraints. Stabilizing excess electron density on a metal adatom or subnanometer metal cluster on metallic substrates requires not only efficient electron donation but also local coordination motifs capable of suppressing rapid charge delocalization into the metallic substrate. Although negatively charged metal centers, e.g., Pt atoms, have been realized in selected environments such as oxide nanostructures,[17] these systems are typically limited in material diversity and lack atomic-scale structural characterization.

On-surface metal−organic coordination[17−29] offers a promising platform to address this challenge, as properly designed organic ligands can simultaneously confine metal adatoms and modulate their electronic states through tailored chemical functionalities. In particular, nitrogen-containing ligands[30−34] can, in favorable geometries, donate electron density to coordinated metal centers and potentially stabilize localized charge accumulation.[35] However, effective electron localization typically requires electronic decoupling from the substrate and is generally facilitated on insulating or weakly interacting supports, whereas controlled assembly, manipulation, and atomic resolution characterization are most readily achieved on metallic substrates. Reconciling these two competing requirements remains a crucial, unresolved challenge.

Here, we demonstrate a surface-coordination strategy that stabilizes atomically well-defined anionic silver adatom dimers on a metallic substrate using a polycyclic aromatic hydrocarbon (PAH) with an NBN unit at the zigzag edge[36,37] on an Ag(100) surface. Following on-surface debromination and

Received: January 15, 2026
Revised: May 19, 2026
Accepted: May 26, 2026

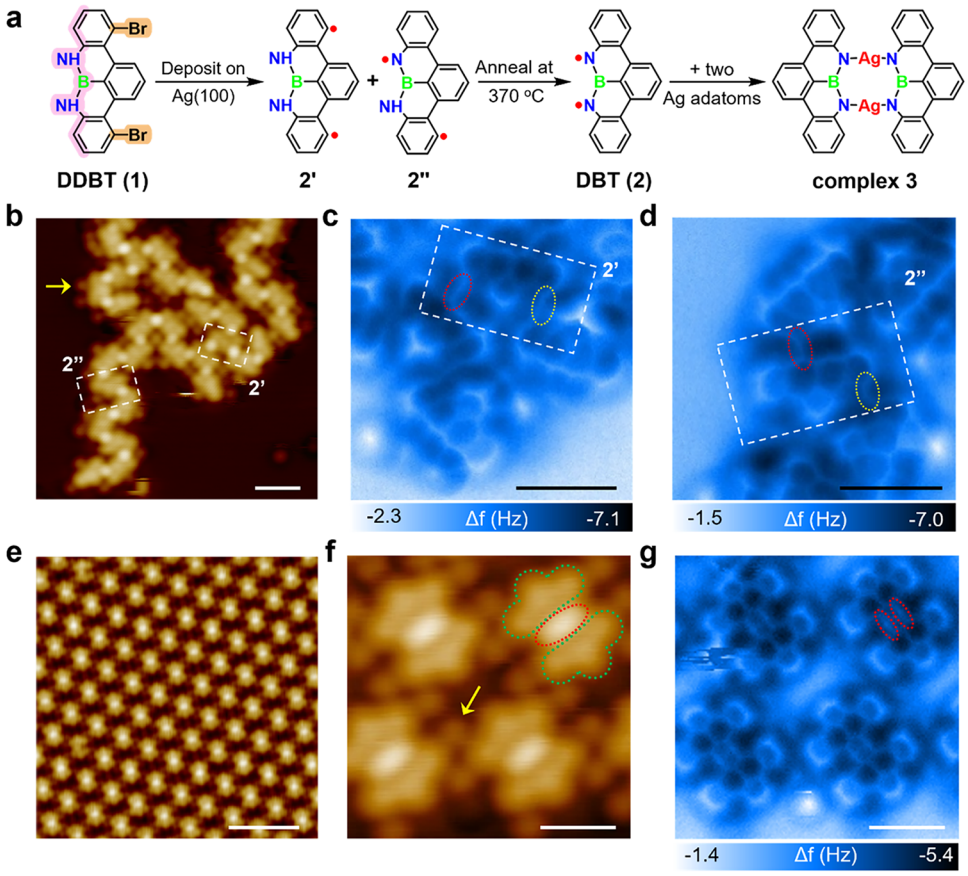

Figure 1. On-surface synthesis and structural characterization of the complex 3 layer with coordinated Ag dimers. (a) Scheme of the synthesis of **3** starting from precursor **1** on Ag(100). (b) Large-scale STM image of **2′** and **2″** on Ag(100) as marked by white rectangles (V_s = 500 mV, I_t = 100 pA). The yellow arrow marks one of the bromine atoms. (c, d) Chemical-bond-resolved nc-AFM images of **2′** and **2″** (oscillation amplitude A_{OSC} = 100 pm). The red and yellow dashed ovals denote C−Ag−N and C−Ag−C bonds, respectively. (e) Large-scale STM image of the complex **3** layer on Ag(100) after annealing at 370 °C (V_s = −40 mV, I_t = 100 pA). (f) Zoom-in STM image of **3** (V_s = −40 mV, I_t = 30 pA). One of the detached Br atoms is indicated by a yellow arrow. The green contours highlight the two DBT monomers in a complex **3**, while the red contour denotes the Ag adatom dimer. (g) Chemical-bond-resolved nc-AFM image taken in the same area of (f) (oscillation amplitude A_{OSC} = 100 pm). The red ovals highlight the two N−Ag−N bonds in complex **3**. Scale bars: (b) 2 nm, (c, d) 1 nm, (e) 5 nm, (f, g) 1 nm.

radical reorganization, biradical monomers coordinate native silver adatoms via N−Ag−N bonds, forming ordered arrays of silver dimers. Combined investigations of noncontact atomic force microscopy (nc-AFM), Kelvin probe force microscopy (KPFM), X-ray photoelectron spectroscopy (XPS), and density functional theory (DFT) calculations confirm the geometry of the coordinated complexes and the negative charge state of the silver adatom dimers ($Ag_2^{\delta-}$). Furthermore, tip-induced removal of one coordinated monomer from the complex enables a controlled conversion of $Ag_2^{\delta-}$ to neutral Ag adatom dimers (Ag_2^0). We further show that CO adsorption is suppressed on the anionic $Ag_2^{\delta-}$ site, providing a single-dimer platform to directly correlate charge state with adsorption behaviors. These results establish an atomically defined platform for stabilizing and controlling anionic metal centers on metallic surfaces, offering new opportunities to investigate charge-state-dependent interactions relevant to surface chemistry and catalysis.

RESULTS AND DISCUSSION

Figure 1a sketches the on-surface synthesis pathway starting from the molecular precursor, 8,9-dibromo-8*H*,9*H*-8,9-diaza-8a-borabenzo[*fg*]tetracene (DDBT, **1**) on an Ag(100) surface. The precursor features two bromine substitutes (outlined in brown) and a zigzag edge embedded in a HN-B-NH (NBN) motif (pink edge in Figure 1a), which together predefine both its surface reactivity and coordination capability. Upon thermal sublimation of DDBT onto an Ag(100) substrate held at room temperature, the precursor (**1**) undergoes spontaneous dehalogenation driven by the catalytic activity of the substrate,[38] giving rise to surface-bound monomer species. As shown in the scanning tunneling microscopy (STM) image in Figure 1b, the resulting monomers assemble into extended structures interconnected by bright protrusions that can be assigned to Ag adatoms. Detached bromine atoms are simultaneously observed in the surrounding regions (indicated by a yellow arrow), appearing with a markedly weaker contrast than the Ag adatoms in the STM image. In bond-resolved nc-AFM images (Figure 1c,d), these Br adatoms appear as distinct bright features at positions consistent with those observed in STM imaging. However, the characteristic high-contrast protrusions associated with C−Br bonds[39,40] are notably absent at the precursor's substitution sites, indicating that debromination has taken place.

A closer inspection of the assemblies identifies two distinct monomers, denoted **2′** and **2″** (Figure 1a), which can be distinguished by the relative position of the Ag adatoms with respect to the molecular backbone of the monomers. In the

https://doi.org/10.1021/jacs.6c00947
J. Am. Chem. Soc. XXXX, XXX, XXX−XXX

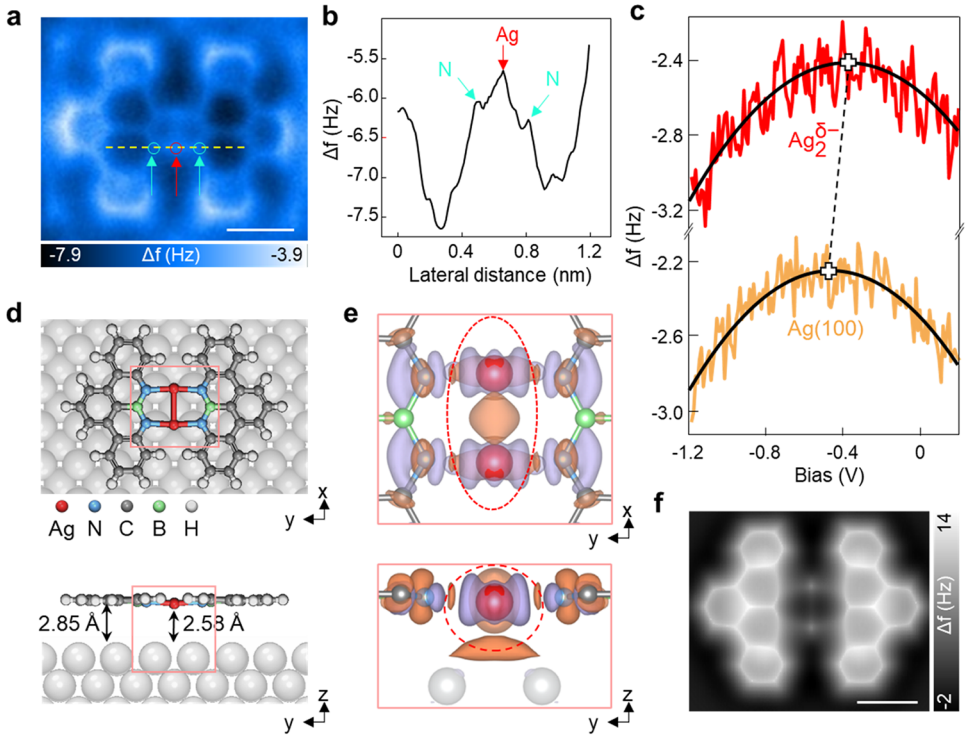

Figure 2. Identification of negatively charged Ag dimers in complex 3. (a) Chemical-bond-resolved nc-AFM image of **3** (resonance amplitude A_{OSC} = 100 pm). The cyan arrows denote the N atoms, and the red arrow denotes the Ag adatom. (b) Line profile along the yellow dashed line in (a), showing a more positive frequency shift on the Ag adatom compared to the N atoms. (c) $\Delta f(V)$ curves on $Ag_2^{\delta-}$ (red curve) and Ag(100) surface (orange curve). The curves are shifted vertically for clarity. LCPD values (black hollow crosses) are extracted from the maximum of fitted parabolic curves (black lines). The black dashed line guides the eye to the difference between them. (d) Top and side views of the DFT-optimized adsorption geometry of **3** on the Ag(100) substrate. (e) Top and side views of the calculated differential charge density between an $Ag_2^{\delta-}$ and the surrounding atoms. The light orange contour shows charge density accumulation, while the light purple contour shows charge density depletion. The isosurface level is 0.03 e/Bohr^3. (f) Simulated nc-AFM images of **3**. Scale bar: (a, f) 0.5 nm.

bond-resolved nc-AFM image of **2′** (Figure 1c), two bonds (C−Ag−N bond in red dashed oval and C−Ag−C bond in yellow dashed oval) extend from the original C−Br sites, indicating that radical character remains localized on both C atoms after debromination. In contrast, a minor population of monomer **2″** (Figure 1d) is also observed, characterized by one bond associated with a nitrogen atom (N−Ag−C bond in red dashed oval) and the other with a carbon atom (C−Ag−C bond in yellow dashed oval). This bonding configuration indicates a partial intramolecular transfer of radical character from carbon to nitrogen, marking an early-stage electronic rearrangement at the NBN-doped zigzag edge.

Upon annealing the sample to 370 °C, the initially short-range-ordered surface-bound intermediates evolve into large-area, well-ordered self-assembled arrays, as shown in Figure 1e. Although the lattice periodicity varies with precursor coverage (Figure S2), the coexistence of multiple superstructures indicates that the assembly is governed primarily by intermolecular interactions rather than by epitaxial registry with the Ag(100) substrate lattice. Despite these lattice variations, all arrays are constructed from an identical structural unit composed of two organic monomers (green dashed contours in Figure 1f) being bridged by a bright, oval-shaped center (red dashed contour in Figure 1f). This central feature is bias-independent, as evidenced in Figure S3, where it remains bright as the scanning bias voltage is varied from +1 V to −1 V. Isolated bromine atoms are also observed between neighboring units, as indicated by the yellow arrow.

Chemical-bond-resolved nc-AFM imaging (Figure 1g) provides direct structural evidence that thermal annealing drives a complete relocation of radical character from carbon to nitrogen, resulting in 8,9-diaza-8a-borabenzo[*fg*]tetracene (DBT, **2**). After annealing, the two DBT monomers within each unit are connected through their nitrogen atoms, indicating the formation of N−Ag−N coordination motifs. The Laplacian-filtered nc-AFM images (Figure S4) clearly reveal a uniform brightness across the coordination sites, which differs from the characteristic low-contrast features and nonplanar geometries typical of radical species.[40,42] The absence of such radical-like signatures indicates the successful formation of the coordination bonds. The presence of two equivalent coordination linkages (red dashed ovals in Figure 1g) indicates that each monomer pair is bridged by two Ag adatoms, thereby establishing a dimeric metal center. These observations unambiguously identify the final product as the coordinated structure depicted as complex **3** in Figure 1a.

DFT calculations reveal a significant thermodynamic driving force (1.37 eV) favoring the spontaneous relocation of radical character from carbon to nitrogen upon annealing (Figure S6). XPS measurements of the N 1s core level were performed both upon **1** deposition and following annealing at 370 °C (Figure S5). For the as-deposited sample, the N 1s peak exhibits a clear split into two components at 399.1 and 397.3 eV, assigned to N−H and N−Ag bonds,[41] respectively. Upon annealing the sample to 370 °C, the component at 397.3 eV increased in intensity, indicating that more carbon radicals transferred to nitrogen radicals, and additional N−Ag bonds were formed.

https://doi.org/10.1021/jacs.6c00947
J. Am. Chem. Soc. XXXX, XXX, XXX−XXX

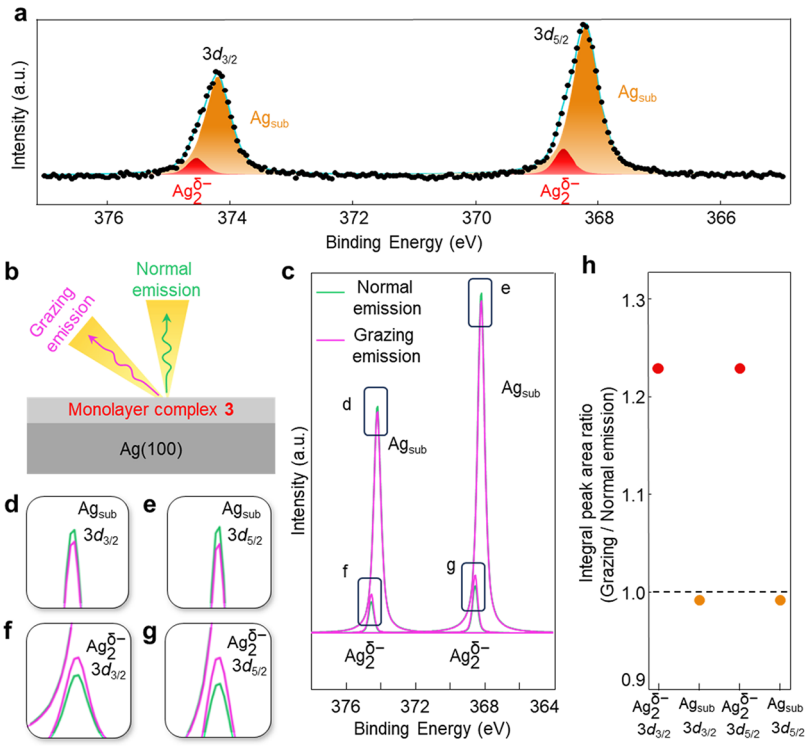

Figure 3. XPS measurements on a full monolayer of complex 3 on Ag(100) substrate. (a) Ag 3d XPS spectra of a monolayer complex **3** on Ag(100) substrate, collected at normal emission. Black dots represent the raw experimental data, the blue line denotes the overall fitted curve, and the peaks were deconvoluted to reflect different contributions, with the orange peaks representing neutral Ag(100) substrate and the red peaks corresponding to $Ag_2^{\delta-}$. (b) Schematic of XPS measurements at different emission angles. (c) Fitting curves of XPS measurement at normal emission (green curve) and grazing emission (purple curve). The peaks of Ag_{sub} $3d_{3/2}$, Ag_{sub} $3d_{5/2}$, $Ag_2^{\delta-}$ $3d_{3/2}$, and $Ag_2^{\delta-}$ $3d_{5/2}$ are displayed in an enlarged view in (d–g) for clarity with the same color code. (h) Integral peak area ratios of grazing/normal emission of Ag 3d spectral components. $Ag_2^{\delta-}$ $3d_{3/2}$ and $Ag_2^{\delta-}$ $3d_{5/2}$ are denoted in red dots, while Ag_{sub} $3d_{3/2}$ and Ag_{sub} $3d_{5/2}$ are in orange.

The thermal stability of the coordinated Ag dimer arrays was examined through annealing to higher temperatures. The arrays remain relatively stable below 400 °C; however, annealing at 440 °C leads to a chemical transformation of the species, resulting in the formation of polymers as characterized by STM and nc-AFM images (Figure S7).

Figure 2 examines the charge state of the Ag atom dimers stabilized within complex **3**. A representative bond-resolved nc-AFM image of an isolated unit is shown in Figure 2a, where the Ag adatoms exhibit a brighter contrast relative to the surrounding N atoms. The corresponding line profile (Figure 2b) along the yellow dashed line in Figure 2a reveals a 0.5 Hz more positive frequency shift on the Ag adatom (red arrow in Figure 2a) than on the coordinating N atoms (cyan arrows), indicating enhanced short-range repulsive interactions measured on the Ag adatoms. For a CO-functionalized tip, metal adatoms with neutral or positive charge typically exhibit a dark halo contrast due to strong attractive electrostatic interactions with the negatively charged O atom at the tip apex.[43−45] Therefore, the observation of a repulsive contrast at the Ag adatoms represents a deviation from this expectation, suggesting an excess negative charge is localized on the Ag dimer.

KPFM measurements were performed on both Ag dimer and Ag substrate using the same CO-terminated tip (Figure 2c). The maxima of the parabolic fittings of the $\Delta f\,(V)$ spectra correspond to the local contact potential difference (LCPD) between the tip and the sample,[46] as marked by the crossings in Figure 2c. The LCPD difference measured above the coordinated Ag dimer (−377 mV, red) is shifted by 81 mV higher than that measured on the Ag(100) substrate (−458 mV, orange). This shift can be interpreted in terms of a dipole moment directed from the vacuum toward the surface, arising from electron accumulation at the coordinated $Ag_2^{\delta-}$, and the associated screening response of the underlying substrate.[7,47,48] In this picture, the induced interfacial dipole increases the effective work function of the Ag(100) substrate region underneath the adatom dimer relative to the pristine surface, which is reflected in the positive shift of the LCPD signal.

Control experiments on Cu(111) reveal that annealing at 200 °C leads to the formation of isolated DBT dimers bridged by Cu adatoms via N−Cu−N coordination (Figure S8a,b). Bond-resolved nc-AFM imaging reveals that the coordinating Cu adatoms exhibit a characteristic dark contrast (Figure S8b,c). Furthermore, KPFM measurements demonstrate that these adatoms possess the same LCPD value as the bare Cu(111) substrate, signifying a neutral charge state (Figure S8d). The fundamental difference between the stabilization of anionic Ag dimers on Ag(100) and the neutral Cu species on Cu(111) is likely attributed to the different work functions of the respective metal substrates.

DFT calculations were performed to elucidate the microscopic origin of the $Ag_2^{\delta-}$ state in complex **3**. In the fully optimized adsorption geometry (Figure 2d), complex **3** adopts a nearly planar configuration, with $Ag_2^{\delta-}$ and DBT (**2**) monomers locating 2.58 and 2.85 Å above the Ag(100) surface, respectively. This adsorption configuration represents the global thermodynamic minimum determined through a

https://doi.org/10.1021/jacs.6c00947
J. Am. Chem. Soc. XXXX, XXX, XXX−XXX

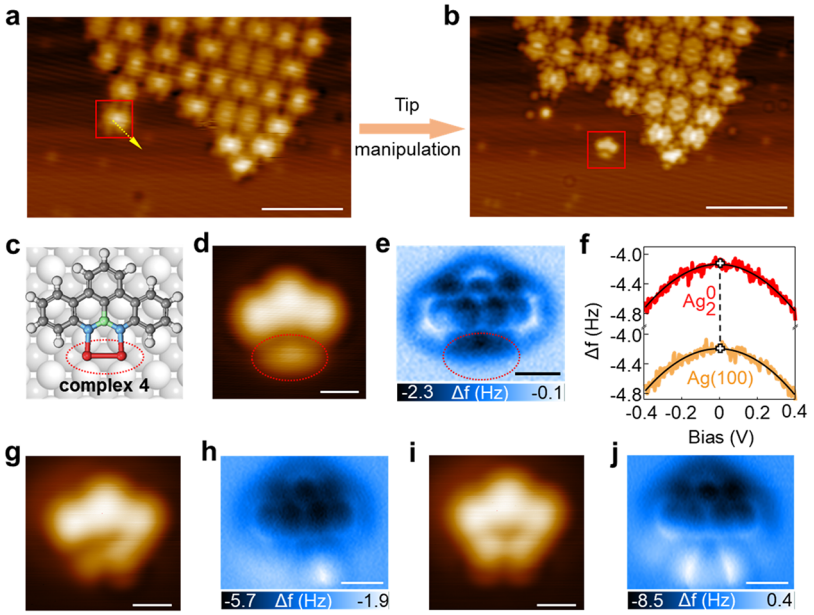

Figure 4. Control the charge state of Ag adatom dimers by tip manipulation. (a, b) Large-scale STM image showing a complex **3** at the edge of an island before and after tip manipulation, as indicated by the red boxes (V_s = −40 mV, I_t = 30 pA). The yellow arrow represents the manipulation path of the tip. (c) Chemical structure of complex **4**. (d, e) Zoom-in STM image (V_s = −40 mV, I_t = 30 pA) and the corresponding chemical-bond-resolved nc-AFM image (A_{OSC} = 100 pm) of **4**. Ag dimer is marked by red dashed ovals. (f) $\Delta f(V)$ curves on the Ag dimer (red curve) and the Ag(100) substrate (orange curve). The curves are shifted vertically for clarity. LCPD values (black hollow crosses) are extracted from the maximum of fitted parabolic curves (black lines). The black dashed line shows that the LCPD values align with each other. (g–j) Zoom-in STM images and nc-AFM images of a complex **4** with one and two CO adsorbates (V_s = −500 mV, I_t = 100 pA, A_{OSC} = 100 pm). Scale bars: (a, b) 5 nm, (d, e) 0.5 nm, (g–j) 0.5 nm.

systematic DFT screening of various high-symmetry sites and molecular orientations (Figure S9). The local coordination environment, characterized by the Ag–N bond length, remains remarkably robust across all tested configurations, indicating that the electronic properties are largely insensitive to minor variations in adsorption registry. Consistent with the DFT results, nc-AFM measurements show that the in-plane N–Ag–N length has slight variations due to local adsorption registry (Figure S10). These geometric fluctuations do not significantly alter the charge transfer between the DBT ligands and the Ag dimer, and the anionic character of the Ag dimer is preserved throughout the array.

Differential charge density (DCD) analysis, shown in Figure 2e, reveals pronounced electron accumulation (light orange) on the Ag adatom dimer and the coordinating nitrogen atoms, as well as at the Ag substrate interface within the region enclosed by the red dashed ovals. Notably, charge depletion (light purple) is observed in the p_y orbitals of the N atoms, indicating that the accumulated electron density localized on $Ag_2^{\delta-}$ primarily donated from the lone-pair electrons of the N atoms. This charge redistribution establishes a net electron transfer from the organic ligands to the Ag dimer, providing a microscopic explanation for its negatively charged character. By calculating the spherical integration of the charge density centered on the Ag adatom and comparing with the bare Ag adatom on the surface, we estimate the transferred charge (δ^-) to be in the range of 0.3 to 1.1 *e*. This interval is bounded by the values integrated at the Ag covalent and van der Waals radii, respectively (Figure S11). Consistent with this picture, calculations of the local electrostatic potential (Figure S12) show a higher potential above the $Ag_2^{\delta-}$ unit than above the Ag(100) substrate, in qualitative agreement with the elevated local potential measured by KPFM on the Ag dimer in complex **3**. Furthermore, a simulated nc-AFM image (Figure 2f) reproduces the enhanced repulsive contrast observed experimentally (Figure 2a), supporting the assignment of $Ag_2^{\delta-}$.

To experimentally resolve the chemical state of the Ag dimer, we prepared a full monolayer of complex **3** on Ag(100), and performed XPS measurements. As shown in Figure 3a, both the Ag $3d_{5/2}$ and $3d_{3/2}$ core levels can be deconvoluted into two components. The dominant peaks (in orange) at 368.20 and 374.20 eV originate from the Ag(100) substrate (Ag_{sub}),[49] whereas the higher-binding-energy shoulders at 368.55 and 374.55 eV are attributed to the $Ag_2^{\delta-}$ species. To further validate this attribution, the Ag 3d core-level spectra obtained from monolayer **3** with $Ag_2^{\delta-}$ species were compared with those from the clean Ag(100) surface (Figure S14). The line shape of the Ag 3d peaks on monolayer **3** exhibits an asymmetry compared to the control samples. The transition from a symmetric line shape in the pristine surface to an asymmetric one in the final assembly indicates that the additional components identified in our peak-fitting analysis can be attributed to the formation of coordinated $Ag_2^{\delta-}$ species. Corresponding core-level shifts (CLS) calculations revealed that $Ag_2^{\delta-}$ exhibits a higher 3d binding energy than neutral surface Ag atoms (Table S2), consistent with the experimental XPS spectra and supporting the assignment of the higher-energy shoulder peak to the surface $Ag_2^{\delta-}$ array.

Emission-angle-dependent XPS measurements were further performed to establish the surface origin of the $Ag_2^{\delta-}$ species, as sketched in Figure 3b. The XPS intensities of Ag_{sub} and $Ag_2^{\delta-}$ at normal and grazing emission are presented in Figure 3c in green and pink curves, respectively, while the peak apexes are magnified in Figure 3d–g. The ratio of grazing to normal emission intensities extracted from the integral peak areas is summarized in Figure 3h. For the Ag(100) substrate, the

https://doi.org/10.1021/jacs.6c00947
J. Am. Chem. Soc. XXXX, XXX, XXX–XXX

normal-emission signal is comparable but slightly more intense than the grazing emission signal (orange dots), consistent with its bulk origin. In contrast, the $Ag_2^{\delta-}$ component exhibits a markedly (more than 1.2 times) enhanced intensity from grazing to normal emission (red dots). The corresponding raw spectra at grazing emission, along with the overlapped raw experimental data at normal and grazing emission, are provided in Figure S15 for reference. This pronounced angular dependence demonstrates that the higher-energy shoulder peak originates from the surface $Ag_2^{\delta-}$ monolayer.

Tip-induced manipulation enables a controlled conversion of the negatively charged $Ag_2^{\delta-}$ in complex **3** into a neutral Ag_2^0 species. Specifically, by laterally sweeping the tip across an individual unit at reduced tip height (yellow arrow, Figure 4a), one DBT monomer (**2**) can be removed from the coordinated motif, yielding complex **4** (red box in Figure 4b,c). This structural modification is accompanied by a pronounced change in the electronic signature of the dimer. In STM images, the Ag_2 feature becomes darker than the surrounding ligand (red dashed oval in Figure 4d). In the corresponding nc-AFM image (Figure 4e), the Ag dimer in complex **4** exhibits only a dark halo contrast dominated by long-range attractions, in clear contrast to the repulsive contrast observed for the negatively charged state.[7,50] Consistently, KPFM measurements show that the LCPD over the Ag_2 site in complex **4** becomes indistinguishable from that of the Ag(100) substrate (Figure 4f). This evidence establishes that $Ag_2^{\delta-}$ in complex **3** loses its excess charge upon tip manipulation and becomes neutral Ag_2^0 in complex **4**.

Our DFT calculations further verify this interpretation (Figure S16). Core-level shift modelings predict a higher Ag 3d binding energy of $Ag_2^{\delta-}$ relative to substrate Ag, whereas the 3d binding energy of Ag_2^0 becomes comparable to that of Ag(100) after removal of one coordination monomer. This DFT binding energy difference well matches the experimentally observed charge-state change from a negatively charged to neutral dimer upon tip-induced structural modification.

The Ag dimers with two charge states exhibit distinct behaviors in CO adsorption. When complex **3** is imaged with a CO-functionalized tip, the CO molecule remains stably bound to the tip apex throughout scanning. In contrast, scanning over complex **4** frequently triggers CO transfers from the tip to the neutral Ag dimer, as demonstrated in Figures 4g–j and S17, indicating a substantially higher affinity of Ag_2^0 toward CO. Once adsorbed, the CO ligand can hop between the two Ag atoms within the neutral dimer and, depending on the scanning conditions, either desorb or yield configurations with one or two CO molecules bound to the Ag_2^0 unit (Figure S17).

This charge-dependent reactivity can be rationalized within the Blyholder framework for CO-metal bonding.[51−53] CO adsorption proceeds through a synergistic interplay of σ donation from the filled 5σ orbital of CO into empty metal s/p states and π backdonation from occupied metal d states into the CO $2\pi^*$ antibonding orbital (Figure S18). For the neutral Ag adatoms, σ donation is efficient, which in turn promotes π backdonation, together stabilizing the Ag-CO bond. In the negatively charged state, however, increased electron density at the metal site strengthens Pauli repulsion against the incoming CO 5σ orbital, suppressing σ donation. Although π backdonation is enhanced, the loss of σ donation breaks the cooperative balance between the two interactions, thereby disfavoring the formation of a stable Ag-CO bond. As a result, CO adsorption is strongly suppressed on $Ag_2^{\delta-}$ while remaining favorable on neutral Ag adatoms. This contrast highlights the critical role of the local coordination environment in governing the electronic structure and adsorption behavior of the adatom dimers, with implications for tuning surface reactivity and selectivity at the atomic scale.

CONCLUSION

In summary, we establish an atomically well-defined monolayer of negatively charged silver adatom dimer $Ag_2^{\delta-}$ on Ag(100), assembled through N−Ag−N coordination with NBN-doped DBT ligands. Our nc-AFM, KPFM, and XPS measurements, together with DFT-calculated DCD, consistently indicate appreciable electron transfer from the DBT ligands to the Ag dimer, giving rise to a negatively charged state. Tip-induced manipulation enables controlled detachment of one coordinating DBT monomer, converting $Ag_2^{\delta-}$ in complex **3** into neutral Ag_2^0 in complex **4**, as evidenced by the contrast reversal in nc-AFM, the disappearance of the LCPD offset in KPFM, and the corresponding trends from DFT core-level shift calculations. The charge state directly affects adsorption behavior, so that neutral Ag_2^0 readily binds CO, whereas CO adsorption is strongly suppressed on $Ag_2^{\delta-}$. These findings establish a controllable strategy for stabilizing and switching the charge state of metal adatom dimers on conductive surfaces, offering a well-defined model platform to interrogate charge-state-dependent adsorption and coordination chemistry at the single-dimer limit.

ASSOCIATED CONTENT

Supporting Information

The Supporting Information is available free of charge at https://pubs.acs.org/doi/10.1021/jacs.6c00947.

Methods, synthesis and characterization of the precursor, DFT calculations on metastable configurations and charge states, XPS spectroscopy on control samples, and STM/nc-AFM images (PDF)

Accession Codes

Deposition Number 2518253 contains the supplementary crystallographic data for this paper. These data can be obtained free of charge via the joint Cambridge Crystallographic Data Centre (CCDC) and Fachinformationszentrum Karlsruhe Access Structures service.

AUTHOR INFORMATION

Corresponding Authors

Li Huang − *Beijing National Center for Condensed Matter Physics and Institute of Physics, Chinese Academy of Sciences, Beijing 100190, China; School of Physical Sciences, University of Chinese Academy of Sciences, Beijing 100190, China*; Email: lhuang@iphy.ac.cn

Wei Ji − *Beijing Key Laboratory of Optoelectronic Functional Materials & Micro-Nano Devices, School of Physics, Renmin University of China, Beijing 100872, China; Key Laboratory of Quantum State Construction and Manipulation (Ministry of Education), Renmin University of China, Beijing 100872, China*; orcid.org/0000-0001-5249-6624; Email: wji@ruc.edu.cn

Xinliang Feng − *Center for Advancing Electronics Dresden (CFAED) & Faculty of Chemistry and Food Chemistry, Technische Universität Dresden, Dresden D-01069,*

https://doi.org/10.1021/jacs.6c00947
J. Am. Chem. Soc. XXXX, XXX, XXX−XXX

Germany; Max Planck Institute of Microstructure Physics, Halle 06120, Germany; Email: xinliang.feng@mpi-halle.mpg.de

Authors

Xiaoshuai Fu − *Beijing National Center for Condensed Matter Physics and Institute of Physics, Chinese Academy of Sciences, Beijing 100190, China; School of Physical Sciences, University of Chinese Academy of Sciences, Beijing 100190, China*

Linlu Wu − *Department of Functional Nanosystems, Interdisciplinary Research Center, Liaoning Academy of Materials, Shenyang 110167, China; Beijing Key Laboratory of Optoelectronic Functional Materials & Micro-Nano Devices, School of Physics, Renmin University of China, Beijing 100872, China; Key Laboratory of Quantum State Construction and Manipulation (Ministry of Education), Renmin University of China, Beijing 100872, China*

Yubin Fu − *Key Lab of Functional Polymers for Sustainability of Jiangsu, School of Energy and Environment, Southeast University, Nanjing, Jiangsu 211189, China; Center for Advancing Electronics Dresden (CFAED) & Faculty of Chemistry and Food Chemistry, Technische Universität Dresden, Dresden D-01069, Germany*; orcid.org/0000-0002-2613-394X

Xiao Chang − *Beijing National Center for Condensed Matter Physics and Institute of Physics, Chinese Academy of Sciences, Beijing 100190, China; School of Physical Sciences, University of Chinese Academy of Sciences, Beijing 100190, China*

Xiaoxiao Pei − *Beijing National Center for Condensed Matter Physics and Institute of Physics, Chinese Academy of Sciences, Beijing 100190, China; School of Physical Sciences, University of Chinese Academy of Sciences, Beijing 100190, China; Hefei National Laboratory, Hefei, Anhui 230088, China*

Chuqi Zhang − *Beijing National Center for Condensed Matter Physics and Institute of Physics, Chinese Academy of Sciences, Beijing 100190, China; School of Physical Sciences, University of Chinese Academy of Sciences, Beijing 100190, China; Hefei National Laboratory, Hefei, Anhui 230088, China*

Chen Liu − *Institute of High Energy Physics, Chinese Academy of Sciences, Beijing 100049, China*

Fupin Liu − *School of Chemistry and Materials Science, Nanjing Normal University, Nanjing 210023, China*; orcid.org/0000-0002-8454-726X

Zhihai Cheng − *Beijing Key Laboratory of Optoelectronic Functional Materials & Micro-Nano Devices, School of Physics, Renmin University of China, Beijing 100872, China; Key Laboratory of Quantum State Construction and Manipulation (Ministry of Education), Renmin University of China, Beijing 100872, China*; orcid.org/0000-0003-4938-4490

Ji Ma − *College of Materials Science and Optoelectronic Technology, University of Chinese Academy of Sciences, Beijing 100190, China*; orcid.org/0000-0003-4418-2339

Xiao Lin − *School of Physical Sciences, University of Chinese Academy of Sciences, Beijing 100190, China*; orcid.org/0000-0002-2490-4691

Hong-Jun Gao − *Beijing National Center for Condensed Matter Physics and Institute of Physics, Chinese Academy of Sciences, Beijing 100190, China; School of Physical Sciences, University of Chinese Academy of Sciences, Beijing 100190, China; Hefei National Laboratory, Hefei, Anhui 230088, China*; orcid.org/0000-0002-6766-0623

Complete contact information is available at: https://pubs.acs.org/10.1021/jacs.6c00947

Author Contributions

[⧖]X.F., L.H., L.W., and Y.F. contributed equally to this work.

Notes

The authors declare no competing financial interest.

■ ACKNOWLEDGMENTS

We acknowledge the financial support from the National Natural Science Foundation of China (Grants No. 62488201, No. 92463307, No. 22572218, No. 92477205, No. 52461160327, No. 52503265, and No. 92477128), the National Key Research and Development Program of China (Grants No. 2024YFA1207700 and No. 2023YFA1406500), the Innovation Program of Quantum Science and Technology (2021ZD0302700), the CAS Project for Young Scientists in Basic Research (YSBR-003), and the CAS Superconducting Research Project (SCZX-0101), Southeast University New Teacher Start-up Fund (4003002508), Hefei Institute of Technology Research Start-up Fund for PhDs and High-Level Talents (2025KY49), and China Postdoctoral Science Foundation (2024M753258). Calculations were performed at the Physics Lab of High-Performance Computing (PLHPC) and the Public Computing Cloud (PCC) of Renmin University of China and the Beijing Super Cloud Computing Center.

■ REFERENCES

(1) Meng, X.; Ma, C.; Jiang, L.; Si, R.; Meng, X.; Tu, Y.; Yu, L.; Bao, X.; Deng, D. Distance Synergy of MoS_2-Confined Rhodium Atoms for Highly Efficient Hydrogen Evolution. *Angew. Chem., Int. Ed.* **2020**, *59* (26), 10502−10507.

(2) Jiang, J.; Ding, W.; Li, W.; Wei, Z. Freestanding Single-Atom-Layer Pd-Based Catalysts: Oriented Splitting of Energy Bands for Unique Stability and Activity. *Chem.* **2020**, *6* (2), 431−447.

(3) Widmann, M.; Niethammer, M.; Fedyanin, D. Y.; Khramtsov, I. A.; Rendler, T.; Booker, I. D.; Hassan, J. U.; Morioka, N.; Chen, Y. C.; Ivanov, I. G.; Son, N. T.; Ohshima, T.; Bockstedte, M.; Gali, A.; Bonato, C.; Lee, S. Y.; Wrachtrup, J. Electrical Charge State Manipulation of Single Silicon Vacancies in a Silicon Carbide Quantum Optoelectronic Device. *Nano Lett.* **2019**, *19* (10), 7173−7180.

(4) Qian, S.; Xu, F.; Fan, Y.; Cheng, N.; Xue, H.; Yuan, Y.; Gautier, R.; Jiang, T.; Tian, J. Tailoring coordination environments of single-atom electrocatalysts for hydrogen evolution by topological heteroatom transfer. *Nat. Commun.* **2024**, *15* (1), No. 2774.

(5) Mohn, F.; Gross, L.; Moll, N.; Meyer, G. Imaging the charge distribution within a single molecule. *Nat. Nanotechnol.* **2012**, *7* (4), 227−231.

(6) Olsson, F. E.; Paavilainen, S.; Persson, M.; Repp, J.; Meyer, G. Multiple charge states of Ag atoms on ultrathin NaCl films. *Phys. Rev. Lett.* **2007**, *98* (17), No. 176803.

(7) Gross, L.; Mohn, F.; Liljeroth, P.; Repp, J.; Giessibl, F. J.; Meyer, G. Measuring the Charge State of an Adatom with Noncontact Atomic Force Microscopy. *Science* **2009**, *324* (5933), 1428−1431.

(8) Repp, J.; Meyer, G.; Olsson, F. E.; Persson, M. Controlling the charge state of individual gold adatoms. *Science* **2004**, *305* (5683), 493−495.

(9) Qi, L.; Babucci, M.; Zhang, Y.; Lund, A.; Liu, L.; Li, J.; Chen, Y.; Hoffman, A. S.; Bare, S. R.; Han, Y.; Gates, B. C.; Bell, A. T. Propane

Dehydrogenation Catalyzed by Isolated Pt Atoms in ≡SiOZn−OH Nests in Dealuminated Zeolite Beta. *J. Am. Chem. Soc.* **2021**, *143* (50), 21364−21378.
(10) Mo, S.; Li, S.; Ren, Q.; Zhang, M.; Sun, Y.; Wang, B.; Feng, Z.; Zhang, Q.; Chen, Y.; Ye, D. Vertically-aligned Co_3O_4 arrays on Ni foam as monolithic structured catalysts for CO oxidation: effects of morphological transformation. *Nanoscale* **2018**, *10* (16), 7746−7758.
(11) Li, J.; Li, Y.; Wang, J.; Zhang, C.; Ma, H.; Zhu, C.; Fan, D.; Guo, Z.; Xu, M.; Wang, Y.; Ma, H. Elucidating the Critical Role of Ruthenium Single Atom Sites in Water Dissociation and Dehydrogenation Behaviors for Robust Hydrazine Oxidation-Boosted Alkaline Hydrogen Evolution. *Adv. Funct. Mater.* **2022**, *32* (16), No. 2109439.
(12) Hannagan, R. T.; Giannakakis, G.; Réocreux, R.; Schumann, J.; Finzel, J.; Wang, Y.; Michaelides, A.; Deshlahra, P.; Christopher, P.; Flytzani-Stephanopoulos, M.; Stamatakis, M.; Sykes, E. C. H. First-principles design of a single-atom−alloy propane dehydrogenation catalyst. *Science* **2021**, *372* (6549), 1444−1447.
(13) Jiang, X.; Zhang, L.; Liu, H.; Wu, D.; Wu, F.; Tian, L.; Liu, L.; Zou, J.; Luo, S.; Chen, B. Silver Single Atom in Carbon Nitride Catalyst for Highly Efficient Photocatalytic Hydrogen Evolution. *Angew. Chem., Int. Ed.* **2020**, *59* (51), 23112−23116.
(14) Gu, J.; Zhao, Y.; Lin, S.; Huang, J.; Cabrera, C. R.; Sumpter, B. G.; Chen, Z. Single-atom catalysts with anionic metal centers: Promising electrocatalysts for the oxygen reduction reaction and beyond. *J. Energy Chem.* **2021**, *63*, 285−293.
(15) Kropp, T.; Lu, Z.; Li, Z.; Chin, Y.-H. C.; Mavrikakis, M. Anionic Single-Atom Catalysts for CO Oxidation: Support-Independent Activity at Low Temperatures. *ACS Catal.* **2019**, *9* (2), 1595−1604.
(16) Yang, J.; Li, W.; Wang, D.; Li, Y. Electronic Metal−Support Interaction of Single-Atom Catalysts and Applications in Electrocatalysis. *Adv. Mater.* **2020**, *32* (49), No. 2003300.
(17) Ji, Y.; Liu, S.; Song, S.; Xu, W.; Li, L.; Zhang, Y.; Chen, W.; Li, H.; Jiang, J.; Zhu, T.; Li, Z.; Zhong, Z.; Wang, D.; Xu, G.; Su, F. Negatively Charged Single-Atom Pt Catalyst Shows Superior SO_2 Tolerance in NO_x Reduction by CO. *ACS Catal.* **2023**, *13* (1), 224−236.
(18) Liu, B.; Miao, G.; Zhong, W.; Huang, X.; Su, N.; Guo, J.; Wang, W. Manipulating the Electronic and Magnetic Properties of Coordinated Nickel Atoms in Metal−Organic Frameworks by Hydrogenation. *ACS Nano* **2022**, *16* (2), 2147−2153.
(19) Zou, H.; Liu, L.; Zhang, S.; Miao, X.; Ying, L.; Deng, W.; Cao, Y. Different Stepwise Growth Mechanism of AIE-Active Tetraphenylethylene-Functionalized Metal−Organic Frameworks on Au(111) and Cu(111) Surfaces. *J. Phys. Chem. Lett.* **2023**, *14* (2), 489−498.
(20) Liu, J.; Li, J.; Xu, Z.; Zhou, X.; Xue, Q.; Wu, T.; Zhong, M.; Li, R.; Sun, R.; Shen, Z.; Tang, H.; Gao, S.; Wang, B.; Hou, S.; Wang, Y. On-surface preparation of coordinated lanthanide-transition-metal clusters. *Nat. Commun.* **2021**, *12* (1), No. 1619.
(21) Liu, J.; Fu, X.; Chen, Q.; Zhang, Y.; Wang, Y.; Zhao, D.; Chen, W.; Xu, G. Q.; Liao, P.; Wu, K. Stabilizing surface Ag adatoms into tunable single atom arrays by terminal alkyne assembly. *Chem. Commun.* **2016**, *52* (88), 12944−12947.
(22) Walch, H.; Dienstmaier, J.; Eder, G.; Gutzler, R.; Schlögl, S.; Sirtl, T.; Das, K.; Schmittel, M.; Lackinger, M. Extended Two-Dimensional Metal−Organic Frameworks Based on Thiolate−Copper Coordination Bonds. *J. Am. Chem. Soc.* **2011**, *133* (20), 7909−7915.
(23) Faraggi, M. N.; Jiang, N.; Gonzalez-Lakunza, N.; Langner, A.; Stepanow, S.; Kern, K.; Arnau, A. Bonding and Charge Transfer in Metal−Organic Coordination Networks on Au(111) with Strong Acceptor Molecules. *J. Phys. Chem. C* **2012**, *116* (46), 24558−24565.
(24) Zhang, Z.; Perepichka, D. F.; Khaliullin, R. Z. Adatoms in the Surface-Confined Ullmann Coupling of Phenyl Groups. *J. Phys. Chem. Lett.* **2021**, *12* (45), 11061−11069.
(25) Yan, L.; Silveira, O. J.; Alldritt, B.; Kezilebieke, S.; Foster, A. S.; Liljeroth, P. Two-Dimensional Metal-Organic Framework on Superconducting $NbSe_2$. *ACS Nano* **2021**, *15* (11), 17813−17819.
(26) Yan, L.; Pohjavirta, I.; Alldritt, B.; Liljeroth, P. On-Surface Assembly of Au-Dicyanoanthracene Coordination Structures on Au(111). *ChemPhysChem* **2019**, *20* (18), 2297−2300.
(27) Weber, P. B.; Hellwig, R.; Paintner, T.; Lattelais, M.; Paszkiewicz, M.; Aguilar, P. C.; Deimel, P. S.; Guo, Y.; Zhang, Y.-Q.; Allegretti, F.; Papageorgiou, A. C.; Reichert, J.; Klyatskaya, S.; Ruben, M.; Barth, J. V.; Bocquet, M.-L.; Klappenberger, F. Surface-Guided Formation of an Organocobalt Complex. *Angew. Chem., Int. Ed.* **2016**, *55* (19), 5754−5759.
(28) Fuhr, J. D.; Robino, L. I.; Rodriguez, L. M.; Verdini, A.; Floreano, L.; Ascolani, H.; Gayone, J. E. 2D Cu-TCNQ Metal-Organic Networks Induced by Surface Alloying. *J. Phys. Chem. C* **2020**, *124* (1), 416−424.
(29) Dong, L.; Sun, Q.; Zhang, C.; Li, Z.; Sheng, K.; Kong, H.; Tan, Q.; Pan, Y.; Hu, A.; Xu, W. A self-assembled molecular nanostructure for trapping the native adatoms on Cu(110). *Chem. Commun.* **2013**, *49* (17), 1735−1737.
(30) Heim, D.; Écija, D.; Seufert, K.; Auwärter, W.; Aurisicchio, C.; Fabbro, C.; Bonifazi, D.; Barth, J. V. Self-Assembly of Flexible One-Dimensional Coordination Polymers on Metal Surfaces. *J. Am. Chem. Soc.* **2010**, *132* (19), 6783−6790.
(31) Nijs, T.; Klein, Y. M.; Mousavi, S. F.; Ahsan, A.; Nowakowska, S.; Constable, E. C.; Housecroft, C. E.; Jung, T. A. The Different Faces of 4′-Pyrimidinyl-Functionalized 4,2′:6′,4″-Terpyridines: Metal−Organic Assemblies from Solution and on Au(111) and Cu(111) Surface Platforms. *J. Am. Chem. Soc.* **2018**, *140* (8), 2933−2939.
(32) Kocić, N.; Liu, X.; Chen, S.; Decurtins, S.; Krejčí, O.; Jelínek, P.; Repp, J.; Liu, S.-X. Control of Reactivity and Regioselectivity for On-Surface Dehydrogenative Aryl−Aryl Bond Formation. *J. Am. Chem. Soc.* **2016**, *138* (17), 5585−5593.
(33) Queck, F.; Kreci, O.; Scheuerer, P.; Bolland, F.; Otyepka, M.; Jelínek, P.; Repp, J. Bonding Motifs in Metal-Organic Compounds on Surfaces. *J. Am. Chem. Soc.* **2018**, *140* (40), 12884−12889.
(34) Lowe, B.; Hellerstedt, J.; Matej, A.; Mutombo, P.; Kumar, D.; Ondrácek, M.; Jelinek, P.; Schiffrin, A. Selective Activation of Aromatic C-H Bonds Catalyzed by Single Gold Atoms at Room Temperature. *J. Am. Chem. Soc.* **2022**, *144* (46), 21389−21397.
(35) Pawin, G.; Wong, K. L.; Kim, D.; Sun, D.; Bartels, L.; Hong, S.; Rahman, T. S.; Carp, R.; Marsella, M. A Surface Coordination Network Based on Substrate-Derived Metal Adatoms with Local Charge Excess. *Angew. Chem., Int. Ed.* **2008**, *47* (44), 8442−8445.
(36) Fu, Y.; Chang, X.; Yang, H.; Dmitrieva, E.; Gao, Y.; Ma, J.; Huang, L.; Liu, J.; Lu, H.; Cheng, Z.; Du, S.; Gao, H.-J.; Feng, X. NBN-Doped Bis-Tetracene and Peri-Tetracene: Synthesis and Characterization. *Angew. Chem., Int. Ed.* **2021**, *60* (50), 26115−26121.
(37) Fu, Y.; Yang, H.; Gao, Y.; Huang, L.; Berger, R.; Liu, J.; Lu, H.; Cheng, Z.; Du, S.; Gao, H.-J.; Feng, X. On-Surface Synthesis of NBN-Doped Zigzag-Edged Graphene Nanoribbons. *Angew. Chem., Int. Ed.* **2020**, *59* (23), 8873−8879.
(38) Bi, X.; Li, C. Editorial: Special Collection of Silver Catalysis in Organic Synthesis. *ChemCatChem* **2021**, *13* (14), 3200−3201.
(39) Wang, D.; Wang, Z.; Liu, W.; Arramel; Zhong, S.; Feng, Y. P.; Loh, K. P.; Wee, A. T. S. Real-Space Investigation of the Multiple Halogen Bonds by Ultrahigh-Resolution Scanning Probe Microscopy. *Small* **2022**, *18* (28), No. 2202368.
(40) Schuler, B.; Fatayer, S.; Mohn, F.; Moll, N.; Pavliček, N.; Meyer, G.; Peña, D.; Gross, L. Reversible Bergman cyclization by atomic manipulation. *Nat. Chem.* **2016**, *8* (3), 220−224.
(41) Haag, F.; Deimel, P. S.; Knecht, P.; Niederegger, L.; Seufert, K.; G Cuxart, M.; Bao, Y.; Papageorgiou, A. C.; Muntwiler, M.; Auwärter, W.; Hess, C. R.; Barth, J. V.; Allegretti, F. The Flexible On-Surface Self-Assembly of a Low-Symmetry Mabiq Ligand: An Unconventional Metal-Assisted Phase Transformation on Ag(111). *J. Phys. Chem. C* **2021**, *125* (42), 23178−23191.
(42) Fritton, M.; Duncan, D. A.; Deimel, P. S.; Rastgoo-Lahrood, A.; Allegretti, F.; Barth, J. V.; Heckl, W. M.; Björk, J.; Lackinger, M. The Role of Kinetics versus Thermodynamics in Surface-Assisted Ullmann

https://doi.org/10.1021/jacs.6c00947
J. Am. Chem. Soc. XXXX, XXX, XXX−XXX

Coupling on Gold and Silver Surfaces. *J. Am. Chem. Soc.* **2019**, *141* (12), 4824−4832.
(43) Ellner, M.; Pavliček, N.; Pou, P.; Schuler, B.; Moll, N.; Meyer, G.; Gross, L.; Peréz, R. The Electric Field of CO Tips and Its Relevance for Atomic Force Microscopy. *Nano Lett.* **2016**, *16* (3), 1974−1980.
(44) Huber, F.; Berwanger, J.; Polesya, S.; Mankovsky, S.; Ebert, H.; Giessibl, F. J. Chemical bond formation showing a transition from physisorption to chemisorption. *Science* **2019**, *366* (6462), 235−238.
(45) Ren, J.; Koy, M.; Osthues, H.; Lammers, B. S.; Gutheil, C.; Nyenhuis, M.; Zheng, Q.; Xiao, Y.; Huang, L.; Nalop, A.; Dai, Q.; Gao, H.-J.; Mönig, H.; Doltsinis, N. L.; Fuchs, H.; Glorius, F. On-surface synthesis of ballbot-type N-heterocyclic carbene polymers. *Nat. Chem.* **2023**, *15* (12), 1737−1744.
(46) Xing, Y.; Shen, J.; Chen, H.; Huang, L.; Gao, Y.; Zheng, Q.; Zhang, Y.-Y.; Li, G.; Hu, B.; Qian, G.; Cao, L.; Zhang, X.; Fan, P.; Ma, R.; Wang, Q.; Yin, Q.; Lei, H.; Ji, W.; Du, S.; Yang, H.; Wang, W.; Shen, C.; Lin, X.; Liu, E.; Shen, B.; Wang, Z.; Gao, H.-J. Localized spin-orbit polaron in magnetic Weyl semimetal $Co_3Sn_2S_2$. *Nat. Commun.* **2020**, *11* (1), No. 5613.
(47) Hiehata, K.; Sasahara, A.; Onishi, H. Local work function analysis of Pt/TiO2 photocatalyst by a Kelvin probe force microscope. *Nanotechnology* **2007**, *18* (8), No. 084007.
(48) Egger, D. A.; Zojer, E. Anticorrelation between the Evolution of Molecular Dipole Moments and Induced Work Function Modifications. *J. Phys. Chem. Lett.* **2013**, *4* (20), 3521−3526.
(49) Firet, N. J.; Blommaert, M. A.; Burdyny, T.; Venugopal, A.; Bohra, D.; Longo, A.; Smith, W. A. Operando EXAFS study reveals presence of oxygen in oxide-derived silver catalysts for electrochemical CO_2 reduction. *J. Mater. Chem. A* **2019**, *7* (6), 2597−2607.
(50) Steurer, W.; Repp, J.; Gross, L.; Scivetti, I.; Persson, M.; Meyer, G. Manipulation of the Charge State of Single Au Atoms on Insulating Multilayer Films. *Phys. Rev. Lett.* **2015**, *114* (3), No. 036801.
(51) Blyholder, G. Molecular Orbital View of Chemisorbed Carbon Monoxide. *J. Phys. Chem. A* **1964**, *68* (10), 2772−2777.
(52) Zhu, W.; Liu, S.; Zhao, K.; Su, Y.; Yang, Y.; Huang, K.; He, Z. Activating *CO by Strengthening Fe−CO π-Backbonding to Enhance Two-Carbon Products Formation toward CO_2 Electroreduction on Fe−N_4 Sites. *Adv. Funct. Mater.* **2024**, *34* (38), No. 2402537.
(53) Perilli, D.; Chesnyak, V.; Ugolotti, A.; Panighel, M.; Vigneri, S.; Armillotta, F.; Naderasli, P.; Stredansky, M.; Schied, M.; Lacovig, P.; Lizzit, S.; Cepek, C.; Comelli, G.; Brune, H.; Africh, C.; Di Valentin, C. CO Adsorption on a Single-Atom Catalyst Stably Embedded in Graphene. *Angew. Chem., Int. Ed.* **2025**, *64* (11), No. e202421757.

https://doi.org/10.1021/jacs.6c00947
J. Am. Chem. Soc. XXXX, XXX, XXX−XXX